UC Davis
UC Davis Previously Published Works

Title

Adaptive-optics optical coherence tomography for high-resolution and high-speed 3D retinal in vivo imaging.

Permalink

Journal

ISSN

Authors

Zawadzki, Robert J
Jones, Steven M
Olivier, Scot S
et al.

Publication Date

DOI

Peer reviewed

Adaptive-optics optical coherence tomography for high-resolution and high-speed 3D retinal in vivo imaging

Robert J. Zawadzki

Department of Ophthalmology and Vision Science, UC Davis, 4860 Y Street, Suite 2400,
Sacramento, California 95817
rjzawadzki@ucdavis.edu

Steven M. Jones and Scot S. Olivier

Lawrence Livermore National Laboratory, 700 East Avenue, Livermore, California 74550

Mingtao Zhao, Bradley A. Bower and Joseph A. Izatt

Department of Biomedical Engineering, Duke University, 101 Science Drive, Durham, North Carolina 27708

Stacey Choi, Sophie Laut and John S. Werner

Department of Ophthalmology and Vision Science, UC Davis, 4860 Y Street, Suite 2400,
Sacramento, California 95817

Abstract: We have combined Fourier-domain optical coherence tomography (FD-OCT) with a closed-loop adaptive optics (AO) system using a Hartmann-Shack wavefront sensor and a bimorph deformable mirror. The adaptive optics system measures and corrects the wavefront aberration of the human eye for improved lateral resolution (~4 μm) of retinal images, while maintaining the high axial resolution (~6 μm) of stand alone OCT. The AO-OCT instrument enables the three-dimensional (3D) visualization of different retinal structures in vivo with high 3D resolution (4x4x6 μm). Using this system, we have demonstrated the ability to image microscopic blood vessels and the cone photoreceptor mosaic.

References and links

1. D. Huang, E. A. Swanson, C.P. Lin, J.S. Schuman, W.G. Stinson, W. Chang, M.R. Flotte, K. Gregory, C.A. Puliafito, "Optical Coherence Tomography," Science **254**, 1178-1181 (1991).
2. A. F. Fercher, C.K. Hitzenberger, G. Kamp, Y. Elzaiat, "Measurement of intraocular distances by backscattering spectral interferometry," Opt. Commun. **117**, 43-48 (1995).
3. M. Wojtkowski, R. Leitgeb, A. Kowalczyk, T. Bajraszewski, A. F. Fercher, "In Vivo human retinal imaging by fourier domain optical coherence tomography," J. Biomed. Opt. **7**, 457-463 (2002).
4. N.A. Nassif, B. Cense, B.H. Park, M.C. Pierce, S.H. Yun, B.E. Bouma, G.J. Tearney, T.C. Chen, J,F. de Boer, "In vivo high-resolution video-rate spectral-domain optical coherence tomography of the human retina and optic nerve," Opt. Express **12**, 367-376 (2004),
http://www.opticsexpress.org/abstract.cfm?URI=OPEX-12-3-367.
5. J.F. de Boer, B. Cense, B.H. Park, M.C. Pierce, G.J. Tearney, and B.E. Bouma, "Improved signal-to-noise ratio in spectral-domain compared with time-domain optical coherence tomography," Opt. Lett. **28**, 2067-2069 (2003).
6. R. Leitgeb, C.K. Hitzenberger, and A.F. Fercher, "Performance of fourier domain vs. time domain optical coherence tomography," Opt. Express **11**, 889-894 (2003),
http://www.opticsexpress.org/abstract.cfm?URI=OPEX-11-8-889.

7. M.A. Choma, M.V. Sarunic, Ch. Yang, J.A. Izatt, "Sensitivity advantage of swept source and Fourier domain optical coherence tomography," Opt. Express **11**, 2183-2189 (2003), http://www.opticsexpress.org/abstract.cfm?URI=OPEX-11-18-2183.

8. R.A. Leitgeb, L. Schmetterer, W. Drexler, A.F. Fercher, R.J. Zawadzki, T. Bajraszewski, "Real-time assesment of retinal blood flow with ultrafast acqusition by color Doppler Fourier domain coherence tomography," Opt. Express **11**, 3116-3121 (2003), http://www.opticsexpress.org/abstract.cfm?URI=OPEX-11-23-3116.

9. Y. Yasuno, S. Makita, Y. South, M. Itoh, and T. Yatagai, "Birefringence imaging of human skin by polarization-sensitive spectral interferometric optical coherence tomography," Opt. Lett. **27**, 1803-1805 (2002).

10. B.H. Park, M.C. Pierce, B.Cense, S.-H. Yun, M. Mujat, G.J. Tearney, B.E. Bouma, J.F. de Boer "Real-time fiber-based multi-functional spectral-domain optical coherence tomography at 1.3 µm," Opt. Express **13**, 3931-3944 (2005), http://www.opticsexpress.org/abstract.cfm?URI=OPEX-13-11-3931.

11. W. Drexler, U. Morgner, R.K. Ghanta, F.X. Kartner, J.S. Schuman, and J.G. Fujimoto, "Ultrahigh-resolution ophthalmic optical coherence tomography," Nature Med. **7**, 502−507 (2000).

12. R. A. Leitgeb, W. Drexler, A. Unterhuber, B. Hermann, T. Bajraszewski, T. Le, A. Stingl, A. F. Fercher, "Ultrahigh resolution Fourier domain optical coherence tomography," Opt. Express **12**, 2156-2165 (2004), http://www.opticsexpress.org/abstract.cfm?URI=OPEX-12-10-2156.

13. B. Cense, N.A. Nassif, T.C. Chen, M.C. Pierce, S.-H. Yun, B. H. Park, B.E. Bouma, G.J. Tearney, J.F. de Boer, "Ultrahigh-resolution high-speed retinal imaging using spectral-domain optical coherence tomography," Opt. Express **12**, 2435-2447 (2004), http://www.opticsexpress.org/abstract.cfm?URI=OPEX-12-11-2435.

14. M. Wojtkowski, V.J. Srinivasan, T.H. Ko, J.G. Fujimoto, A. Kowalczyk, J.S. Duker, "Ultrahigh-resolution, high-speed, Fourier domain optical coherence tomography and methods for dispersion compensation," Opt. Express **12**, 2404-2422 (2004), http://www.opticsexpress.org/abstract.cfm?URI=OPEX-12-11-2404.

15. D.T. Miller, J. Qu, R.S. Jonnal, and K. Thorn, "Coherence gating and adaptive optics in the eye," in *Coherence Domain Optical Methods and Optical Coherence Tomography in Biomedicine VII*, V.V. Tuchin, J.A. Izatt, J.G. Fujimoto, eds., Proc. SPIE **4956**, 65-72 (2003).

16. B. Hermann, E.J. Fernandez, A. Unterhubner, H. Sattmann, A.F. Fercher, and W. Drexler, P.M. Prieto and P. Artal, "Adaptive-optics ultrahigh-resolution optical coherence tomography," Opt. Lett. **29**, 2142-2144 (2004).

17. Y. Zhang, J. Rha, R.S. Jonnal, D.T. Miller, "Adaptive optics parallel spectral domain optical coherence tomography for imaging the living retina," Opt. Express **13**, 4792-4811 (2005), http://www.opticsexpress.org/abstract.cfm?URI=OPEX-13-12-4792.

18. J. Liang, D.R. Williams and D.T. Miller, "Supernormal vision and high-resolution retinal imaging through adaptive optics," J. Opt. Soc. Am. A **14**, 2884 (1997).

19. A. Roorda, F. Romero-Borja, W.J. Donnelly III, H. Queener, T.J. Hebert, and M.C.W. Campbell, "Adaptive optics scanning laser ophthalmoscopy," Opt. Express **10**, 405-412 (2002), http://www.opticsexpress.org/abstract.cfm?URI=OPEX-10-9-405.

20. J. Carroll, D.C. Gray, A.Roorda, D.R. Williams, "Recent advances in retinal imaging with adaptive optics," Opt. Photon. News **16**, 36-42 (2005).

21. F. Romero-Borja, K. Venkateswaran, A. Roorda, and T.J. Hebert, "Optical slicing of human retinal tissue in vivo with adaptive optics scanning laser ophthalmoscope," Appl. Opt. **44**, 4032-4040 (2005).

22. R.J. Zawadzki, B.A. Bower, M. Zhao, M. Sarunic, S. Laut, J.S. Werner and J.A. Izatt, "Exposure time dependence of image quality in high-speed retinal in vivo Fourier-domain OCT," in *Ophthalmic Technologies XV*, F. Manns, P.G. Soederberg, A. Ho, B.E. Stuck, M. Belkin, eds., Proc. SPIE **5688**, 45-52 (2005).

23. ANSI, *American National Standard for the Safe use of* Lasers, ANSI Z136.1 (Laser Institute of America, Orlando, FL, 2000).

24. D.A. Horsley, H. Park, S.P. Laut, J.S. Werner, "Characterization for vision science application of bimorph deformable mirror using phase-shifting interferometry," in *Ophthalmic Technologies XV*, F. Manns, P.G. Soederberg, A. Ho, B.E. Stuck, M. Belkin, eds., Proc. SPIE **5688**, 133-143 (2005).

25. E. Dalimier, Ch. Dainty, "Comparative analysis of deformable mirrors for ocular adaptive optics," Opt. Express **13**, 4275-4285 (2005), http://www.opticsexpress.org/abstract.cfm?URI=OPEX-13-11-4275.

26. R.K. Tyson, *Principle of Adaptive Optics* (Academic Press, inc., 1991), Chap. 7.

27. L. Diaz-Santana, C. Torti, I. Munro, P. Gasson, Ch. Dainty, "Benefit of higher closed-loop bandwidths in ocular adaptive optics," Opt. Express **11**, 2597-2605 (2003), http://www.opticsexpress.org/abstract.cfm?URI=OPEX-11-20-2597.

28. R.W. Rodieck, *The Vertebrate Retina* (W.H. Freeman, San Francisco, 1973).

29. E.J. Fernández, A. Unterhuber, P.M. Prieto, B. Hermann, W. Drexler, P. Artal, "Ocular aberrations as a function of wavelength in the near infrared measured with a femtosecond laser," Opt. Express **13**, 400-409 (2005), http://www.opticsexpress.org/abstract.cfm?URI=OPEX-13-2-400.

30. J.I. Yellott Jr, "Spectral analysis of spatial sampling by photoreceptors: Topological disorder prevents aliasing," Vision Res. **22**, 1205-1210 (1982).

31. Ch.A. Curcio, K.R. Sloan, R.E. Kalina, A.E. Hendrickson "Human Photoreceptor Topography," J Comp. Neurol. **292**, 497-523 (1990).

1. Introduction

Optical coherence tomography (OCT) in the time domain [1] has become an essential tool in the diagnosis and monitoring treatment of human retinal disease. This imaging modality has recently been improved by Fourier-domain OCT (FD-OCT) [2-4] because it offers a significant advantage in sensitivity and acquisition speed over the standard time-domain OCT technique [5-7]. The high speed of Fourier-domain OCT permits the 3D imaging of in vivo retinal structures. More recent attempts to acquire functional data have also been demonstrated with Doppler FD-OCT [8], polarization-sensitive FD-OCT [9] as well as multifunctional systems [10].

Although development of novel light sources [11-14] has improved axial resolution for retinal imaging below 3 µm in both time-domain and Fourier-domain systems, substantially less work has been conducted to improve lateral resolution to theoretical diffraction-limited performance. Nowadays, most OCT systems used for retinal imaging are still limited to transverse resolution of approximately 15 to 20 μm. Two reports of improved lateral resolution for time-domain OCT have been published by Miller et al. [15] using en face coherence-gated OCT and by Hermann et al. [16] using UHR-OCT. Moreover, a first attempt to implement AO correction in Fourier-domain OCT imaging has been reported recently by Zhang et al. [17], based upon novel line illumination, parallel FD-OCT to image photoreceptors on single B-scans.

This investigation used an adaptive optics system deploying a Hartmann-Shack wavefront sensor and deformable mirror operating in a closed loop. This approach to improve the transverse resolution for retinal imaging has already been demonstrated in other retinal imaging modalities, first in standard AO-fundus cameras and more recently in AO-scanning laser ophthalmoscopes (AO-SLO) [18-20]. The latter modality allows real-time observation of microscopic retinal structures in human eyes, including the photoreceptor cone mosaic, nerve fiber layer and microscopic blood flow in capillaries [21-22]. Due to the limited axial resolution of these systems, they cannot be used to image other retinal layers or to create detailed 3D reconstructions of retinal volume which is a key advantage associated with OCT imaging.

In this paper, we describe a hybrid AO-OCT instrument, successfully combining the advantages of real-time FD-OCT and the advanced technology for adaptive optics, using a 35-element bimorph deformable mirror (DM) as a wavefront-corrector. Our approach differs from that described in previous reports because we use the OCT imaging beam to record and correct wavefront-aberrations allowing truly real-time operation of AO correction and elimination of additional light sources. Another feature of our system is the incorporation of a bimorph DM from AOptix as a wavefront corrector which has an exceptionally high dynamic range and hence the ability to correct large amounts of defocus and other low-order aberrations, eliminating the need for trial lenses to correct individual subject's refractive errors up to ± 3 diopters defocus range.

Correction of ocular aberrations with our AO-OCT instrument decreases the lateral size of the point-spread function (PSF) while maintaining axial resolution as well as high speed and real-time data display and acquisition of a stand alone FD-OCT. The first images acquired with this system including 3D volume imaging show the great potential of this novel instrument for vision science and clinical applications.

2. Materials and methods

The AO-OCT system presented in this paper occupies 1x1 m of a standard laboratory optical table. The sample arm utilizes a Hartmann-Shack wavefront sensor and a 35-electrode bimorph deformable mirror for aberration correction. A key advantage of our system is that the same light source is used for both OCT and Hartmann-Shack detection channels, allowing simultaneous operation of AO and OCT. Two independent PCs were used, one for AO

control (AO-PC) and one for the OCT scanning and detection unit (OCT-PC). Separate sample and reference arms were constructed on the same table to test the OCT system with and without AO. A bite-bar, forehead-rest assembly was mounted on an X-Y-Z translation stage to permit precise positioning of the subject's eye. An image from the wavefront sensor was used to monitor the X-Y position of the eye's pupil while fixation was directed to an external target to minimize head and eye motion and to allow precise imaging of different retinal locations. To ensure the maximum pupil size and minimize fluctuations in accommodation, the subject's eye was dilated and cyclopleged with 2.5% Phenylephrine and 1% Tropicamide.

2.1 Fourier-domain OCT

The Fourier-domain OCT system [22] presented in this paper used the spectral OCT approach in which a high-efficiency spectrometer measures the spectrum of the light that returns from reference and sample arms. A standard fiber-based OCT instrument is operated in Michelson interferometer configuration, where FC/APC fiber connectors are used to connect the fiber coupler's (80/20 splitting ratio) two outputs to fiber collimators placed at the input of bulk optics of the sample and reference arms. This feature of our OCT engine (light source, fiber coupler, detection channel) allows interchangeable operation for both AO-OCT and standard OCT imaging. Two sample arms and two reference arms were constructed for AO-OCT and OCT imaging. Simple reconnection of FC/APC fiber connectors allows rapid switching between the two systems. Figure 1 shows a schematic of the OCT engine.
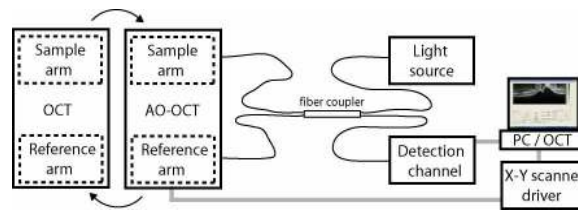

Fig. 1. Schematic of the OCT engine used in our experiments. Black lines - fiber connections; gray lines - electrical connections. Two separate sample and reference arms permit switching between OCT and AO-OCT imaging systems. The splitting ratio of the fiber coupler was 80/20 (reference/sample)

2.1.1 Theory

In order to gain access to depth information carried by back-scattered light from the sample arm it must be combined with light back-reflected from the reference arm, consisting of a mirror placed at the proper optical path length, and sent to the detection channel where the spectral interference pattern is recorded. This spectral information, as seen by the spectrometer's CCD camera, can be described as [4]:

$$I(k) = I_r(k) + I_s(k) + 2\sqrt{I_r(k)I_s(k)} \sum_n \alpha_n \cos(k z_n) \tag{1}$$

where $I_r(k)$, $I_s(k)$ refer to wavelength-dependent intensities from reference and sample arms, respectively; k is wave number; and, α_n is the square root of sample reflectivity at depth z_n. The depth information (equivalent of A-scan in time-domain) is accessed by FTT^{-1} of the spectrometer signal:

$$I(z) = \left| FT^{-1}[I(k)] \right|^2 = \Gamma^2(z) \otimes \left\{ \delta(0) + \sum_n \alpha_n^2 \delta(z \pm z_n) + O[I_s^2 / I_r^2] \right\} \tag{2}$$

where $\Gamma(z)$ is the envelope of the coherence function. To remove the autocorrelation term $\delta(0)$ and "coherence artifacts," $O[I_s^2/I_r^2]$ in Eq. 2, we use DC subtraction already described by other groups [13-14]. To overcome the problem of the complex conjugate image present after implementation of the Inverse Fourier Transform, we display only one half the image and place the whole retina on a negative path length difference side with respect to the reference mirror position.

2.1.2 Detection channel

As already noted, the light from the sample and reference arms is split in the fiber coupler and sent via fiber to the detection channel consisting of a science grade custom-built spectrometer. At the input of this channel the light is collimated using a 100 mm focal length collimating objective (OZ optics) and sent to the 1200 l/mm holographic transmitting diffraction grating (Wasatch Photonics). A custom-design objective (triplet) having 150 mm focal length is used to focus the light onto the CCD. The detection spectrometer uses a CCD line-scan camera (12 bit, Atmel, 2048-pixels) which samples the spectrum with 0.066 nm spectral spacing, $\delta\lambda$. The OCT computer is a dual processor Intel Xeon 3.6 GHZ with 3GB RAM memory. The standard system settings allow acquisition rates varying from 9 Frames/s (1000 A-scans/Frame; 100 μs exposure) to 36 Frames/s (500 A-scans / Frame; 50 μs exposure). Custom C++ based software developed at Duke University fully processes (including re-sampling from λ to k, dispersion compensation to third order, and FFT), displays, and streams B-scan data to system memory in real time at the same frame rates, allowing the operator to track and eliminate streamed data affected by eye motion or eye blinking. Two main scanning settings for 3D image acquisition were used: 100 B-scans/volume (with 1000 A-scans/B-scan) and 200 B-scans/volume (with 500 A-scans/B-scan). In both cases, the full volume acquisition time was less then 6 s for 50 μs A-scan exposures. After finishing acquisition, depending on our scanning pattern settings, the raw data of the last 100 or 200 frames are optionally streamed to the PC's hard drive. These data may be later post-processed in LabVIEW using numerical dispersion compensation methods previously described by Wojtkowski et al [14] and zero-padding techniques [4] to further enhance image quality. With the current spectrometer design, the maximum axial range (seen after Fourier Transform) is 2.7 mm in free space, corresponding to approximately 2 mm in the eye.

2.1.3 Experimental

The heart of the OCT engine is a fiber-based Michelson interferometer. Two light sources, superluminescent diodes (SLD) from Superlum (λ_0 = 841 nm, $\Delta\lambda$ = 50 nm, P = 8 mW) and (λ_0 = 890 nm, $\Delta\lambda$ = 140 nm, P = 7.3 mW) were used, with estimated axial resolution of Δz = 6 μm and 3.5 μm, respectively, in the retina. The spectrum of the first SLD was imaged on 1024 pixels of our CCD while the second one used all 2048 pixels. The power at the subject's eye was 400 μW for the AO-OCT system and 700 μW for the OCT system, below the ANSI maximum recommended exposure levels [23].

The reference DC file was updated before each test to remove the coherent noise in our images. An OCT/PC drives the two x- and y-galvo scanners allowing different scanning modes: standard B-scans, radial, circular as well as 3D acquisition for both AO-OCT and OCT instruments. In this paper, however, we present only B-scans and 3D scanning acquisition patterns.

2.2 Adaptive Optics

The AO system is positioned in the sample channel of the AO-OCT instrument between the fiber and subject's eye. The main advantage of this approach is that the imaging beam is corrected before entering the eye and on the exit path from the eye to the detector. This ensures equal spot size and imaging resolution with the most efficient light usage. One of the drawbacks of this approach is the requirement of a long reference arm to match the sample

arm length; in our case, it is equal to about 7 m. The AO-control software used in our system was developed at the Lawrence Livermore National Laboratory. Figure 2 shows a schematic of our AO system control.
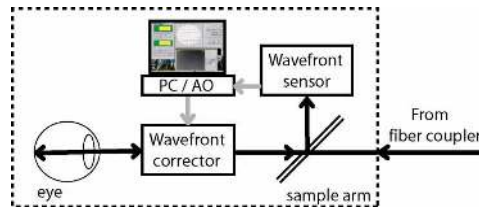

Fig. 2. Schematic of the AO - control system used in our experiments. Black lines represent light paths and gray denotes electrical connections.

2.2.1 Wavefront Sensing

The AO-control computer (PC/AO) reads the data from the Hartmann-Shack wavefront sensor (the combination of a lenslet array and a CCD camera placed in its focal plane) and uses it as a reference for wavefront correction. The sensor is a Dalsa 1M60 CCD CameraLink camera with a 20x20 lenslet array (Adaptive Optics Associates, 0500-30-S-A) having 500-μm pitch and 30 mm focal length. The circular array of the 284 lenslets, used as shown by Fig. 3, is at a conjugate plane with the eye pupil and sees the 8% of the OCT light back-reflected from the retina that is redirected by a 8/92 pellicle beam-splitter. The eye pupil plane is magnified 1.44 times so that the wavefront at the pupil plane is sampled with center-to-center spacing of 348 μm. The wavefront sensor measures centroids, i.e., displacements of the spots produced by the lenslet array from its reference position. These values are then multiplied by a control matrix that determines the array of voltages to drive the actuators of the deformable mirror. The control matrix is calculated as an inverse of the system matrix measured experimentally. Since we are using closed-loop adaptive optics in our instrument, the centroid values from the wavefront sensor are measured at the beginning of each loop and are then used to find new (updated) voltage values to shape the deformable mirror. This system operates at 25 Hz; the global control loop performs the correction of aberrations with the same temporal frequency.

2.2.2 Wavefront Compensation

A 35-element, bimorph DM from AOptix Technologies, Inc is used as the wavefront corrector. It consists of two layers of ceramic lead magnesium niobate (PMN) that are directly actuated by the electrodes bonded on the material. PMN material deforms when an electric field is applied, allowing total stroke of ~32 μm. Performance of this mirror for ophthalmic applications has been recently tested by Horsley et al [24] and Dalimier et al. [25]. The magnification factor, γ, between the eye pupil plane and DM planes was based upon the physical dimensions of the wavefront corrector and equals 1.43 for the AOptix DM (10 mm diameter pupil image). Figure 3 illustrates the geometry of active elements of our deformable mirror with respect to the scaled pupil size. Note that even though only 19 inner actuators (curvature deformation actuators) of the bimorph mirror are covered by the image of the pupil, all 35 elements of the DM including 16 outer ring actuators (slope actuators) are used to correct the wavefront.
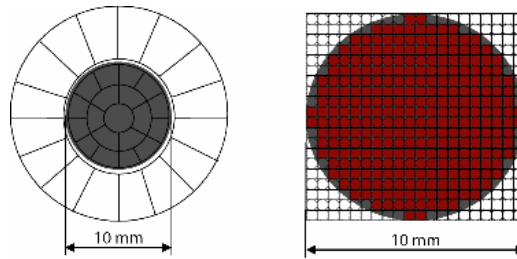
Fig. 3. Actuator geometry for the 35-element AOptix DM (left) and Hartmann-Shack 400-lenslet configuration (right). The gray area corresponds to an image of a 7 mm eye pupil diameter. Note different scales for DM and lenslet array. Red circles on the right image indicate "active" spots used for wavefront calculation.

Our initial tests demonstrated that the AOptix bimorph DM is capable of correcting relatively large defocus and spherical aberrations owing to its maximum stroke of $\pm$ 16 μm. However, as the order of Zernike modes increases, there is an increase in the residual wavefront error. Moreover, superposition of different Zernike modes tends to reduce even more dramatically mirror performance for higher-order modes. Despite these problems, we decided to use this large stroke of the DM to introduce arbitrary amounts of defocus to shift the focal plane of our imaging instrument while still correcting the remaining aberrations. This proved to be an important feature of our instrument because only the depth range on the order of 50-60 μm (for diffraction-limited performance with pupil diameter of 6-7 mm) is located in the near field of the focusing spot and offers the best lateral resolution. Thus, to exploit the superior lateral resolution of our AO-OCT system, the focal plane of the instrument should be shifted towards the structure of interest. As a rule of thumb, one-quarter diopter of defocus shifts the focal plane on the retina by ~93 μm. Another important advantage of using the DM for shifting focus is that the path length in the sample arm stays constant. This is critical for imaging with FD-OCT where any change in the sample arm length would shift the image and force the operator to compensate for it by moving the mirror in the reference arm. In our case, no active compensation is necessary. Our current AO-control software allows seven predefined settings of the DM to create arbitrary defocus in the pupil plane, which was sufficient to shift the focus through all retinal layers of interest. The result of shifting focus is an increase in intensity due to better coupling of reflected light from the imaged structures.

The control of the deformable mirror for AO requires the use of the classical singular value decomposition (SVD) method, already well described in the literature [26], to generate the set of voltages associated with the reconstruction of a specific wavefront.

2.3 UC Davis AO-OCT instrument

The optical design of the sample arm consists of a series of afocal telescopes that conjugate the eye pupil plane with all key components of the system: x and y scanning mirrors (which limits scanner motion error observed on the wavefront sensor), the bimorph deformable mirror and the Hartmann-Shack wavefront sensor. Our AO-OCT system was designed with spherical mirrors, instead of lenses commonly used in OCT sample arms, to reduce dispersion matching problems as well as back reflections that can occur while the scanners are moving (which may reduce performance of the H-S wavefront sensor). One of the problems with such a design is that spherical mirrors are used in off-axis configuration which introduces static aberration. This problem is reduced by using mirrors with long focal lengths.
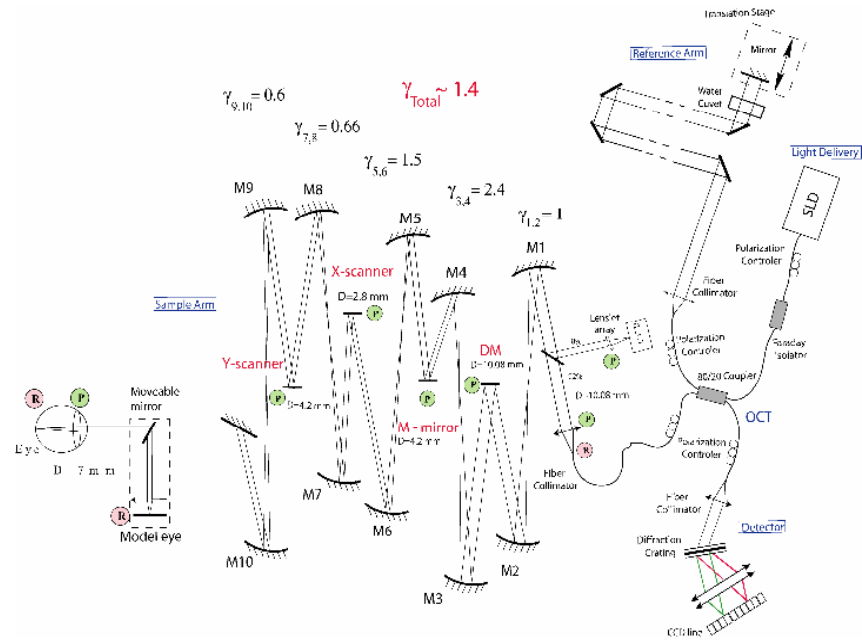
Fig. 4. Schematic of UC Davis AO – OCT experimental setup constructed on a standard laboratory optical table occupying 1x1 m. The reference arm length has been shortened on the illustration for simplification. Key: γ - magnification, D - diameter, DM – deformable mirror; M1-M10 – spherical mirrors, P – pupil plane, R - retinal plane.

The scanning field of view of our current instrument allows us to image up to ± 1.5 deg or 1 mm patches of retina, as compared to ± 12 deg or 8 mm scanning range commonly used in commercial instruments (Stratus OST, Carl Zeiss Meditec). This value has been chosen due to the limited isoplanatic angle for the human eye. A schematic of the optical elements is shown in Fig. 4. As already mentioned, lack of back reflections allows simultaneous wavefront measurement and correction during OCT system operation to compensate for some dynamic ocular aberrations that would otherwise compromise OCT image quality [27]. To match the dispersion of the sample arm, a water vial (25 mm length) is placed in the reference arm.

3. Results and discussion

To date more than 60 individuals have been tested with our OCT instrument and 15 with AO-OCT. All images presented here were acquired from the eyes of healthy volunteers whose age ranged from 20 to 50 years. One consideration in choosing these individuals was their relatively low level of involuntary eye motion, which is an important factor for successful 3D volumetric imaging.

3.1 OCT

The performance of our stand-alone OCT system (with standard "shorter" sample arm) was tested for retinal imaging prior to incorporating it into the AO-OCT system. Figure 5 shows the resultant high-resolution image ($\Delta z = 3.6$ µm) acquired over 6 mm centered on the fovea. We also present our labeling of retinal layers based primarily upon light microscopy [28] and results of our clinical trials. Note that there is unequal scaling of axial and lateral dimensions of these images to conform with convention in displaying OCT retinal images. This image established the adequacy of our stand-alone OCT system and can be use as a reference for AO-OCT images.
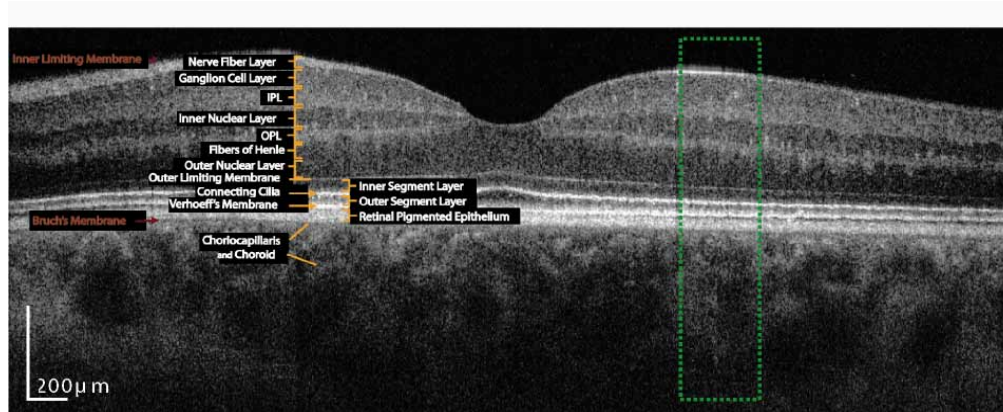
Fig. 5. High-resolution B-scan of retinal structures acquired with our OCT instrument scanning 6 mm lateral range (4000 A-scans). We have identified the following retinal layers based on comparison with the literature: Nerve Fiber Layer (NFL), Ganglion Cell Layer (GCL), Inner Plexiform Layer (IPL), Inner Nuclear Layer (INL), Outer Plexiform Layer (OPL), Fibers of Henle with Outer Nuclear Layer (ONL), Inner Segment Layer (ISL), Outer Segment Layer (OSL), Retinal Pigment Epithelium (RPE), Choriocapillaris and Choroid. The Outer Limiting Membrane (sometimes called External Limiting Membrane), Connecting Cilia and Verhoeff's Membrane may also be seen. The Fibers of Henle cannot be distinguished from the ONL in this image. The Inner Limiting Membrane and Bruch's Membrane are also not visible on this image but have been confirmed using the same OCT system for imaging diseased retinas. The green rectangle denotes the scanning range of 500 µm used by our AO-OCT system when imaging at an eccentricity of 4 deg temporal retina (TR).

The rectangular frame shown on the right side of the picture represents an example of the scanning area of 500 μm located at 4 deg temporal eccentricity as imaged by our AO-OCT system. As can be seen, the AO-OCT instrument can image only a fraction of the retinal area seen by standard OCT systems.

3.2 AO-OCT

The purpose of incorporating AO into our OCT engine is to improve lateral resolution. To reduce effects of chromatic aberration of the eye [29], we used the Superluminescent diode (λ_O = 841 nm, $\Delta\lambda$ = 50 nm, P = 9 mW) allowing 6-µm axial resolution. All of the results shown in this section have been acquired with 50 μs line exposure time.

3.2.1 AO testing

To test the AO-system performance we measured and corrected known aberrations of the model eye (introduced by trial lenses placed in front of it) with a paper used as a scattering model of the retina. These experiments demonstrate excellent ability of our DM to correct low-order aberrations, defocus (up to ±3 diopters) and cylinder (up to ±1 diopters). Next, the AO-system was tested for wavefront measurement and correction in the human eye *in vivo*. These experiments confirmed the system's ability to correct low- and high-order aberrations. Figure 6 shows an example of reconstructed wavefronts before and after AO correction, as measured in vivo for one of our subjects, together with total wavefront RMS error over time. As can be seen, our AO system can significantly compensate aberrations and maintain low RMS wavefront error during its closed-loop operation. The ability to correct wavefront error in real time, while imaging, allows compensation of the eye's temporal aberration fluctuations. To better estimate the performance of our wavefront corrector, the Zernike representation of the reconstructed wavefront has been calculated and analyzed. Figure 7 shows the Zernike coefficients associated with the wavefront presented in Fig. 6. A clear reduction in the low-order aberration modes is observed.
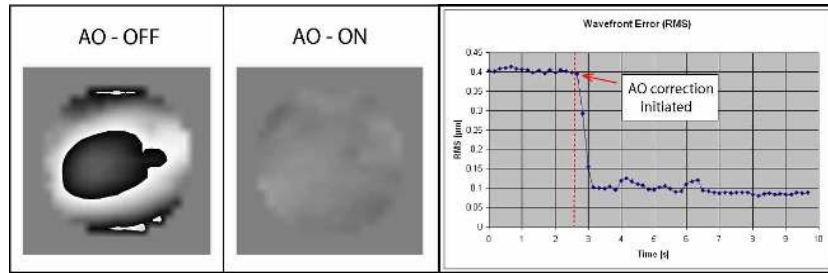
Fig. 6. The ocular wavefront measured by H-S wavefront sensor before (left) and after (center) AO-correction. Left and center images present the reconstructed PSF for these wavefronts. Right plot shows total wavefront RMS error over time as measured by the H-S wavefront sensor before and during correction. The RMS error was corrected at a rate of 25 Hz but is displayed at rate of 6 Hz.
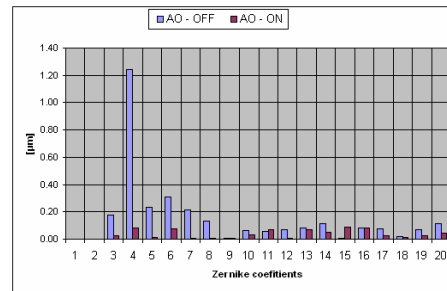

Fig. 7. Reconstructed Zernike coefficients measured before (blue) and during (red) AO correction. Numbers correspond to the following Zernike coefficients: second-order aberrations: 3,5 – astigmatism, 4 – defocus; third-order aberrations: 6,9 – trefoil, 7,8 – coma; fourth- order aberrations: 10,14 – tetrafoil, 11,13 – 2nd astigmatism, 12 – spherical aberrations; fifth-order aberrations 15-20

3.2.2 Retinal imaging

Figure 8 shows a real-time image sequence of the retinal B-scans of a healthy 20-year-old volunteer, acquired with AO-OCT during initiation of AO correction. This image was acquired at a rate of 18 Frames/s at 4 deg temporal retina (TR) and covers 1 mm.
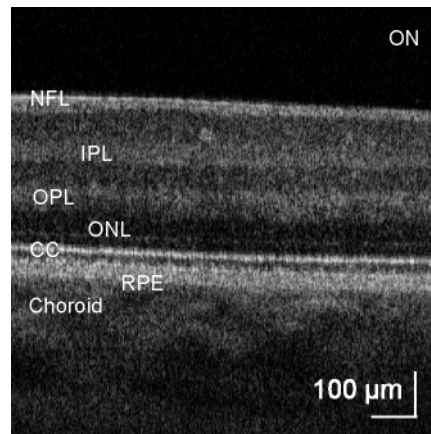

Fig. 8 (1.34 MB) Real-time movie of retina acquired with AO-OCT during initiation of AO correction. The image covers 1x1 mm (1000 A-scans / Frame). (5.15 MB version)

A clear improvement in image brightness as well as better visualization of retinal structures can be observed with AO correction. This is probably due to the large amount of defocus and astigmatism that have been corrected by the DM. Some of these low-order aberrations are associated with the refractive error of the imaged eye (no trial lenses are used in our system) and residual system aberrations. To test the effect that defocus may have on image intensity, we imaged the retina while forcing our DM to introduce small amounts of defocus.
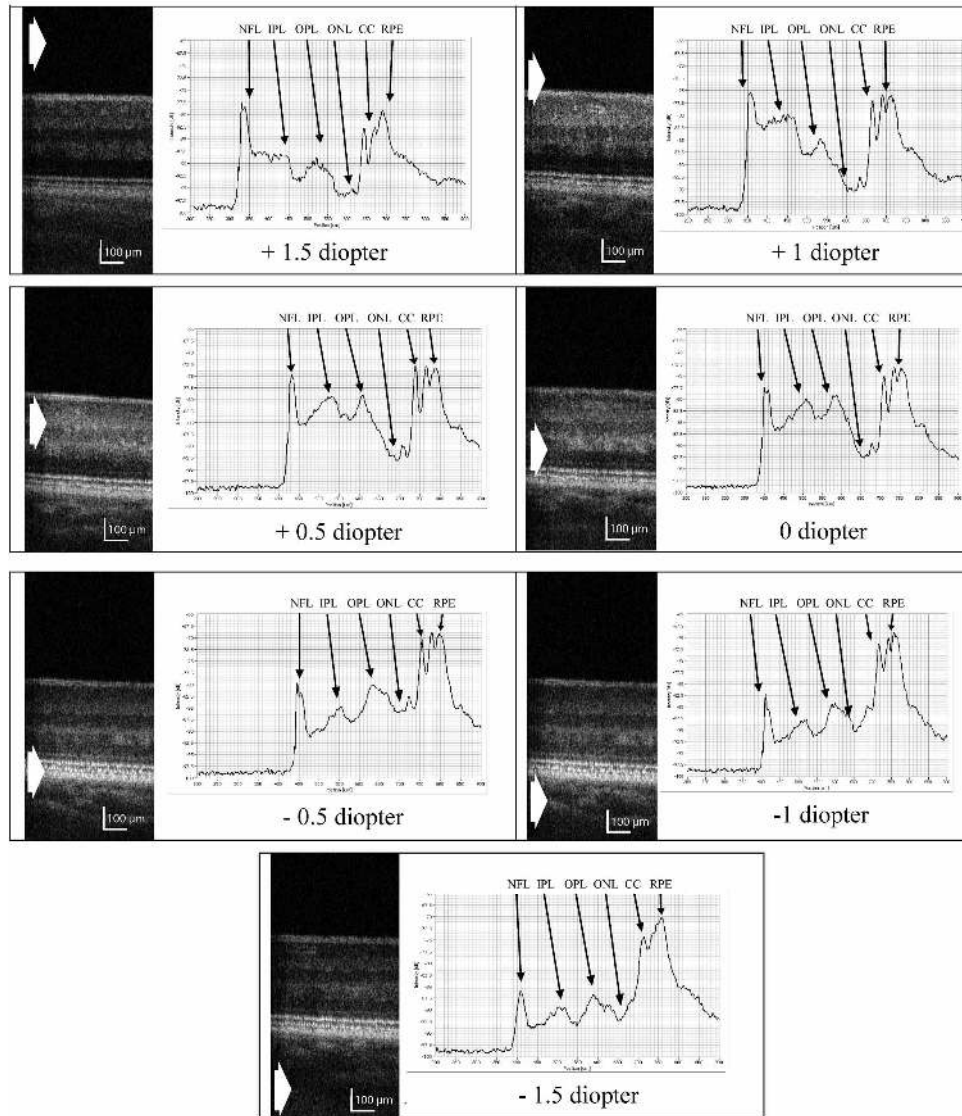

Fig. 9. In vivo OCT images of AO-corrected retinal structures with axial intensity profiles for seven different focusing positions (both in logarithmic scale). The narrow depth of focus manifests itself by increases in intensity of the structures at the beam focus. All images have been acquired over 500 μm lateral distance. The effect of shifting the plane of focus on B-scans is illustrated. A white arrow marks the position of the focus plane on retinal structures. The image covers 0.5 x 1mm, comprising 512 x 500 pixels of original data (depth x width). The vertical axes are scaled identically for all intensity profiles and range from -65 dB (top limit) to -100 dB (lower limit) in sample reflectivity.

Theoretical calculation shows that 1 diopter defocus should shift the focal plane on the retina about 370 µm for the standard eye. Figure 9 shows the effect of residual defocus on image quality for seven DM-defocus values (while still correcting higher-order aberrations) programmed in our AO-control system. As can be seen in Fig. 9, a clear change in the intensity profile is associated with shifting the focal plane. This observation correlates with the theoretical prediction of ~93 µm focal plane shift for each quarter diopter of defocus. Moreover, it is clear that in our system, maximum performance (high sensitivity and lateral resolution) can be achieved over a depth range of approximately plus/minus 50 µm surrounding the focus position. Based on these results we estimate the sensitivity of our AO-OCT system to be around -97 dB in focus and dynamic range on the order of 30 dB. Thus, to exploit the superior lateral resolution of our AO-OCT system, the focal plane of the instrument should always be shifted towards the structure of interest. The tilt in the retinal structure is due to eccentric fixation.

3.2.3 3D imaging

Volumetric retinal imaging was used to visualize the performance of our AO-OCT system. To reduce time between consecutive B-scans (and hence eye motion artifacts), most of our images were acquired in a high-speed volumetric imaging mode comprising 200 B-scans/volume with 500 A-scans/B-scan. Thus, the time needed to acquire the entire 3D structure (for 50 µs A-scan exposure time) was less then 6 s. The images were acquired over a 0.5 x 0.2 mm rectangular area of retina with 1 µm lateral sampling density in both lateral directions (between A-scans and B-scans). Before 3D reconstruction, all frames were registered in a semi-automatic way for axial eye motion. No post processing has been used to reduce blur associated with lateral eye motion. The first 100 A-scans of each frame (B-scan) have been removed due to artifacts caused by the vibration of our scanners (A saw-tooth signal was used to drive both X- and Y-scanners). For these data we did introduce +0.5 diopters defocus by the DM; thus, the system focus was on the upper layers of retina.

To visualize our volumetric data we used a custom software package for 3D-OCT visualization developed in collaboration with the Institute for Data Analysis and Visualization at the UC Davis Department of Computer Science. Figure 10 shows a movie of a 3D representation of the retina structure.
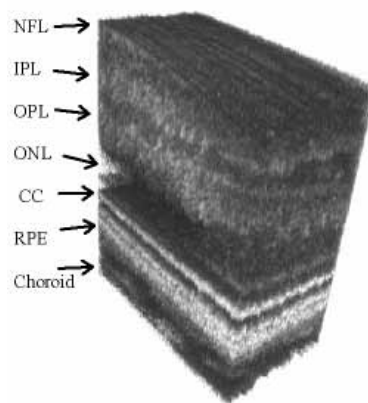

Fig. 10. (1.3 MB) Movie presenting 3D visualization of microscopic retinal structure reconstructed from 200 laterally displaced B-scans (with 500 A-scans/B-scan) covering 400x200x800 µm (lateral x lateral x depth). The focus position was set on the upper retinal layers (+0.5 diopter). (14.3 MB version)

Because standard B-scan representations of OCT images do not fully illustrate the improved resolution of AO-OCT (even though some microscopic structures are clearly visible), we have examined C-scans reconstructed from 3D volume rendering of B-scans. The figure below shows a movie sequence of the C-scan (flat illumination) reconstructed from the 3D volume acquired over a 1x1mm lateral area with 100 B-scans (at 1000 A-scans/B-scan). There was no defocus introduced by the DM in this case; thus, the system focus was on the photoreceptor layers.
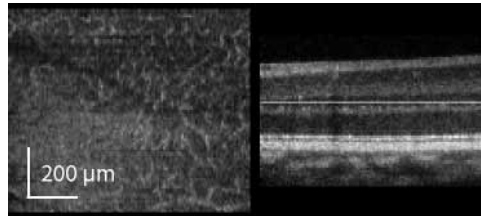

Fig. 11. (0.98 MB) Movie sequence of the C-scan (flat illumination) reconstructed from the 3D volume 1000x100x512 voxels (lateral x lateral x depth). The white line on the B-scan (right) corresponds to the position of the reconstructed C-scan (left). C-scan image size: 1x1mm (3x3 deg) (lateral sampling = 1 μm between A-scan and 10 μm between B-scans), eccentricity of 6 deg nasal retina. (7.36 MB version)

As seen on Fig. 11, C-scan reconstruction of our volumetric data reveals lateral structures at different retinal layers. For example, note the dense network of small blood vessels in the two plexiform layers. We estimate the diameter of these capillaries to be on the order of 10-20 μm, making them visible even though the focus of our system has been shifted to other retinal layers. The key factors allowing imaging of these structures is dense lateral sampling and probably reduction of lateral speckle sizes by use of a high NA in our imaging system.

To quantitatively estimate the effect of AO correction on lateral resolution, and to correlate some of the observed structures with known quantitative cellular profiles, different analytical methods have been applied. For example, one of the standard procedures to quantify photoreceptor density in AO-flood illumination systems is by the 2D FFT power spectra of *en-face* images [30]. In the case of reconstructed C-scans, no clear spatial component similar to the ring observed on power spectra of photoreceptor mosaics of AO-fundus images has been found. However, for Connecting Cilia (Inner/Outer segment junction) in the photoreceptor layer, a 2D power spectrum demonstrated the periodic structures of the B-scan direction (fast line acquisition) and a blurred one on the vertical (slow) axis. This asymmetric effect is probably due to the lateral motion of the eye causing distortion seen on the C-scans of the original images. This blurs the spectral components of structures lying between different B-scans.

To evaluate the lateral spacing of the structures in the different retinal layers, a one-dimensional Fourier analysis, as proposed by Zhang et al. [17], has been applied to our reconstructed C-scans. Hence, a 1D power spectrum was calculated for each "fast axis" line of a C-scan and then an averaged power spectrum was obtained from all 200 FFTs (200 fast axis lines). This analysis was repeated for each retinal depth (reconstructed C-scan). Next, these results were used to create a 2D intensity profile of the power spectrum representing spatial frequency components of each retinal layer.
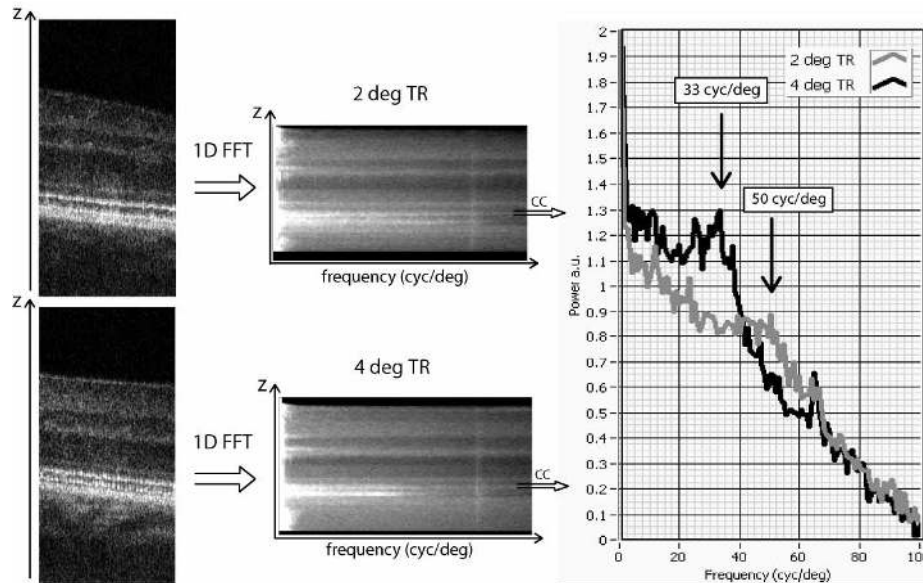
Fig. 12. B-scans taken from the volumetric data (left) with corresponding 1D averaged power spectrum (center) (calculated from C-scans). The data have been acquired at two different retinal eccentricities, 2 deg (upper) and 4 deg (lower) temporal retina (TR). Central graph shows intensity encoded averaged 1D power spectrum calculated at each retinal depth revealing the presence of regular structures in both plexiform layers (capillaris), photoreceptor layers and choriocapillaris and choroid. Right graph shows 1D power spectrum at connecting cilia for the two retinal locations. Arrows indicate the spatial frequency corresponding to the peaks in the power spectra. The values of 33 cyc/deg and 50 cyc/deg correspond to spacings of 10 μm and 6.7 μm respectively, between imaged structures.

The results of this analysis for two volumetric data sets (200x500x512) acquired at two different retinal locations are shown by Fig. 12. Note a spectral component in the power spectrum corresponding to the photoreceptor layer (at the Connecting Cilia and Verhoeff's membrane). This was also noted in both plexiform layers and in the choroid. This is due to the regular structures seen on the C-scans. We then compared averaged 1D power spectra of two C-scans acquired on the same depth (at Connecting Cilia) at different eccentricities. Shifts in lateral spacing of the spatial frequency (50 cyc/deg at 2 deg TR and cyc/deg at 4 deg TR) correlate with cone-to cone spacing observed in AO-flood illumination systems as well as that reported for cone photoreceptor mosaics by Curcio et al. [31]. Some discrepancy may be expected due to anatomical variation of photoreceptor spacing between different subjects as well as by scaling errors of AO-OCT. Nevertheless, we submit that the structures seen in the imaged photoreceptor layers are cone photoreceptors. Moreover, based on the measurements of spatial frequency of imaging structures we estimate the lateral resolution of our system be in the order of 4 μm during AO correction.

4. Conclusion

The performance of the AO-OCT system presented in this paper is similar to that described by other groups using time-domain as well as line-illumination Fourier-domain AO-OCT. That is, there is an increase in the system sensitivity during AO operation (manifested as a change in image brightness) probably mainly due to reduction of defocus and astigmatism. High acquisition speed of FD-OCT allows for the first time the 3D data collection and further C-scan image evaluation which may be important for the comparison of AO-OCT system findings with other imaging instruments (e.g., flood-illumination AO and AO-SLO). Initial testing demonstrates excellent correction of low-order optical aberrations using the bimorph

DM, but an additional DM may be necessary to better correct the higher-order aberrations. Strong horizontal motion artifacts can be seen on all reconstructed C-scans due to the nature of our imaging technique (fast acquisition of B-scans). Thus the C-scan frame rate in our system is equal to the 3D acquisition rate and therefore is slow compared to C-scan based imaging techniques (transversal OCT, SLO). However, one of the main advantages of this approach is relatively simple implementation of axial eye motion correction, allowing visualization of thin retinal layers and junctions between layers.

Due to the coherent nature of the detection method used in OCT, a speckle noise (manifesting itself as a "sand" structure superimposed on the image) will always be present while imaging scattering objects such as the retina. One of the physical parameters defining speckle is its average size, which is comparable to the theoretical PSF size of the imaging instrument. Therefore, the smaller the structure (closer to the resolution limit of the system), the more evident is the effect of the noise. It is apparent from the movies presented in this paper that temporal averaging may be one of several methods that will be helpful in solving this problem.

Acknowledgments